6-1-2009

Computation vs. Experiment for High-Frequency Low-Reynolds Number Airfoil Plunge

Michael V. Ol

Mark F. Reeder
Air Force Institute of Technology

Daniel Fredburg

Gregory Z. McGowan

Ashok Gopalarathnam

See next page for additional authors

Recommended Citation

Ol, M. V, et al. (2009). Computation vs. Experiment for High-Frequency Low-Reynolds Number Airfoil Plunge. International Journal of Micro Air Vehicles, 1(2), 99–119. https://doi.org/10.1260/175682909789498279

Computation vs. Experiment for High-Frequency Low-Reynolds Number Airfoil Plunge[a]

Michael V. Ol[b], Mark Reeder[c] and Daniel Fredberg[d], Gregory Z. McGowan[e] , Ashok Gopalarathnam[f], Jack R. Edwards[g]

[a]Professor Tomonari Furukawa served as Editor-in-Chief during this article

[b]Aerospace Engineer, Air Force Research Laboratory Air Vehicles Directorate, Michael.Ol@wpafb.af.mil

[c]Associate Professor, , Air Force Institute of Technology, Dept. of Aeronautics and Astronautics

[d]Graduate student, Air Force Institute of Technology, Dept. of Aeronautics and Astronautics

[e]Doctoral Candidate, North Carolina State University, Dept. of Mechanical and Aerospace Engineering

[f]Associate Professor, North Carolina State University, Dept. of Mechanical and Aerospace Engineering

[g]Professor, North Carolina State University, Dept. of Mechanical and Aerospace Engineering

Received on 8 November 2008; Accepted on 16 January 2009

ABSTRACT

We seek to extend the literature on sinusoidal pure-plunge of 2D airfoils at high reduced frequency and low Reynolds number, by including effects of camber and nonzero mean incidence angle. We compare experimental results in a water tunnel using dye injection and 2D particle image velocimetry, with a set of computations in 2D – Immersed Boundary Method and unsteady Reynolds-Averaged Navier Stokes. The Re range is from 10,000 to 60,000, based on free stream velocity and airfoil chord, chosen to cover cases where transition in attached boundary layers would be of some importance, and where transition would only occur in the wake. Generally at high reduced frequency there is no Reynolds number effect. Mean angle of attack has significance, notionally, depending on whether it is below or above static stall. Computations were found to agree well with experimentally-derived velocity contours, vorticity contours and momentum in the wake. As found previously for the NACA0012, varying Strouhal number is found to control the topology of the wake, while varying reduced amplitude and reduced frequency together, but keeping Strouhal number constant, causes wake vortical structures to scale with the reduced amplitude of plunge. Flowfield periodicity – as evinced from comparison of instantaneous and time-averaged particle image velocimetry - is generally attained after two periods of oscillation from motion onset.

NOMENCLATURE

f	=	plunge physical frequency
k	=	reduced plunge frequency, $k = \pi fc/U_\infty$
U_∞	=	free-stream velocity
h	=	non-dimensional plunge amplitude
c	=	airfoil chord, =152.4 mm
x/c	=	airfoil chord fraction
Re	=	Reynolds number based on c and U_∞
St	=	Strouhal Number, $St = 2fc/U_\infty = 2kh/\pi$
φ	=	phase of motion
$\hat{t}$	=	non-dimensional time
C_L	=	lift coefficient

A = angle of attack
α_T = total effective angle of attack due to plunge
α_0 = airfoil mean geometric incidence angle

1. INTRODUCTION

Plunging airfoils are useful and common abstractions in unsteady aerodynamics for a wide range of applications in low-speed flight, such as helicopter rotors[1]. The motivation of the present work, and the point of departure from classical unsteady airfoil theory[2] and classical dynamic stall[3], is aerodynamic modeling for Micro Air Vehicles (MAVs) of all three types – fixed-wing, rotary-wing, and flapping-wing. The small size and low flight speed of MAVs necessarily leads to high dimensionless rates of motion, either intentional (aggressive maneuver, wing rotation for "perching", wing flapping in hover and loiter) or unavoidable (response to gusts of high amplitude relative to the vehicle flight speed). The desired underlying knowledge set is how the flowfield and integrated aerodynamic coefficients – lift, drag/thrust, and pitch – vary with angle of attack time history. Periodic, and in particular sinusoidal angle of attack variation, is the most attainable and most commonly studied realization in practical laboratory settings. One can ask how the flowfield relaxes to periodicity upon onset of the forced oscillation[4], and how the flowfield varies from period-to-period once nominal periodicity is attained. Even in the case of strong periodicity, the question is how aerodynamic response lags motion kinematics – that is, to what extent does this response depart from quasi-steady. Matters are further complicated by laminar separations at low Reynolds number, where even in steady airfoil aerodynamics one finds that $C_L = f(\alpha)$ exhibits unusual behavior[5].

The MAV application, where $C_L>0$ is important, suggests a cambered airfoil with good on-design performance at MAV-relevant Reynolds numbers; the Selig SD7003 airfoil was chosen because of prior work on the static case[14]. Pure-plunge of the SD7003 airfoil at Re = 60,000 at reduced frequency $k \leq 0.80$ was studied by Radespiel et al.[6], to compare the suction-side boundary layer transition and laminar separation bubble between weakly-unsteady and static cases[16]. High-frequency sinusoidal pure-plunge of a NACA 0012 spanning across the test section, at zero mean angle of attack, has become something of a standard problem, with an extensive literature. Examples include the extensive series of studies by Lai and Platzer[7] and Jones et al.[8], where the focus was on thrust-production and wake structure for various combinations of reduced frequency and reduced amplitude; and more recently using particle image velocimetry, by Ellenrieder and Pothos[9].

Plunging motion is defined in Equation (1) with resulting angle of attack time history given in Equation (2) and maximal extent of angle of attack given in Equation (3).

$$h(t) = h_o cos(2\pi ft) \tag{1}$$

$$\alpha(t) = \alpha_o + arctan\,[2\pi fch\,(t - \tfrac{\pi}{2})/U_\infty] = \alpha_o + arctan\,[2kh\,(t - \tfrac{\pi}{2})] \tag{2}$$

$$\alpha_T = \alpha_o \pm arctan\,[2kh_o]. \tag{3}$$

Following a plunge-case studied by Lai and Platzer[7], we take k = 3.93 (note the factor of 2 difference in definition of k between the present definition and that of ref.[7]) and h = 0.05.

By comparing experiment and computation, we seek validation in both directions. Blockage in the water tunnel has been suspected as a nontrivial source of discrepancy relative to unbounded domains[10], and the present implementation of the plunge rig is expected to be intrusive. The experiment would also be expected to suffer from free-surface effects, free-stream turbulence and flowfield nonuniformity, and deviations between attained and prescribed motion kinematics. Computations, of course, have their own challenges of turbulence and transition modeling and in the present case of limitations to 2D, of proper treatment of wall-effects, grid refinement and so forth. RANS-type computations for periodic $\alpha(t)$ are necessarily periodic, which raises question of error if the physical flow departs from periodicity. The hope is that favorable comparison between experiment and computation is not merely fortuitous coincidence, but evidence that the various errors of either approach are nevertheless small enough to support validity of at least qualitative conclusions of trends in flowfield response vs. change in this or that parameter. The use of 3D computational meshes and a stereoscopic PIV measurements are long-term goals but are beyond the scope of the current study.

2. EXPERIMENTAL SETUP

2.1. Water Tunnel

Dynamic testing in water offers advantages of relatively low physical motion rates for a given reduced rate, simplification in tares of inertial vs. aerodynamic effects, and simplicity of flow visualization by passive markers (dye) nominally tracking shed vortical structures.[11,12] The present experiments were performed at the Air Force Research Laboratory Air Vehicles Directorate's "Horizontal Free-Surface Water Tunnel" (HFWT), Wright Patterson Air Force Base (WPAFB). The test section is 0.46 m x 0.61 m x 2.74 m, with a free-surface and a surface skimmer plate isolating the intake plenum from the test section. The contraction ratio is 4:1, with two honeycomb screens and three wire-mesh screens in the settling chamber. A 12" axial impeller, driven by a 15 hp motor, gives a flow velocity range of approximately 3.8 to 45 cm/s. Single-component hot-film measurements evince a stream wise turbulence intensity of approximately 0.1 percent.[13] The HFWT and the approach used for airfoil PIV measurements are described in more detail in Ol et al.[14]

2.2. Motion Control Rig

Though the present work is limited to plunge normal to the free-stream direction, the forced-oscillation rig is capable of pitch and plunge. Thus, the airfoil motion was driven by a 2-degree-of-freedom pitch-plunge rig, consisting of a pair of electric model H2W A-40-series linear servomotors mounted vertically on a plate above the tunnel test section free-surface. The model is supported along its midspan by two vertical rods and mounted upside down in order to collect data on the low pressure side of the airfoil without free surface effects on the laser sheet propagation. Each motor actuates a vertical rod, which connects via a bushing to the airfoil at a fixed pivot point on the airfoil chord. Motion trajectory of each rod is programmed independently, allowing for single degree-of-freedom motions such as sinusoidal pure-pitch or pure-plunge, as well as nontrigonometric and combined motions. Additional details of the pitch-plunge rig is given in Ol[15].

The HFWT's motion control rig is not unique, but does depart from more common approaches taken in water tunnels. Briefly, examples of other 2DOF rig designs (Figure 1) include those described by Paquet[16] (top mount, two-component actuation at model end, with wing piercing free-surface), Parker, Soria and von Ellenrieder[17] (top mount with pitch and plunge on separate carriages), Anderson et al[18]. (end-mounts, model horizontal with pitch and plunge on separate stages), Hanff[16] (center mount, pair of hydraulic actuators, similar to the present design), and Kurtulus et al.[19] (end-mount, separate pitch and plunge carriages).

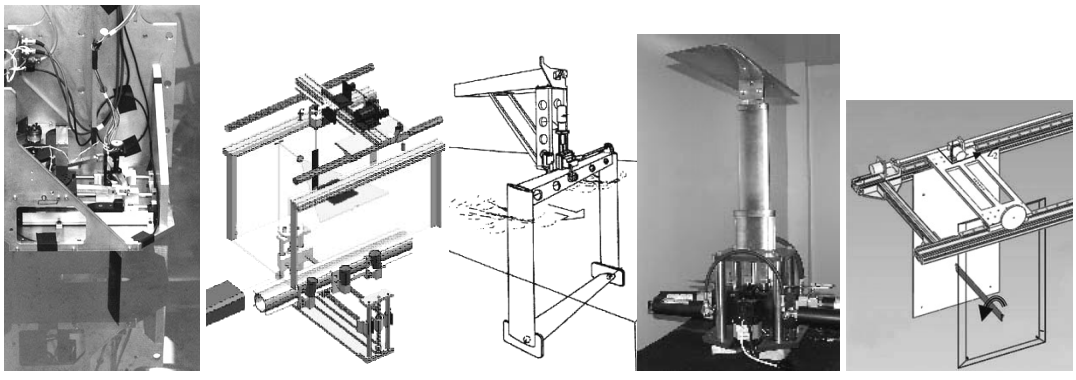

(a) **(b)** **(c)** **(d)** **(e)**

Figure 1. Examples of 2-degree-of-freedom pitch-plunge rigs in water tow-tanks and water tunnels: (a) Paquet[16], (b) Parker et al.[17], (c) Anderson et al.[18], (d) Hanff[16], and (e) Kurtulus et al.[19]

One 2DOF airfoil oscillation system design trade is supporting a vertically-hanging model from one tip, with the other free or abutting the test section floor; or, connecting to both tips, with the model horizontal; or, a center-mount system with struts connecting to the centerline of a horizontal model. The first has advantages of placing the force balance above the water line and thus solving the balance waterproofing issues, and has the least interference between the rig struts and the model flowfield. However, it makes free-surface effects largely unavoidable. The model mass (physical mass and motion-induced apparent mass) produces an unbalanced load on the model supports, which is especially troublesome for large models oscillating at high speeds in liquids. The second is limited to rigid airfoil models spanning the tunnel test section. The third keeps model loads balanced and allows for both wall-to-wall models and wings of various planform, but has large disadvantages of rig strut interference with the flowfield. This, however, is to some extent of secondary importance if particle image velocimetry data are taken in planar slices well-away from the model centerline. Assuming that this assertion is true, a center-mounted arrangement was selected.

Actuation options include rotary servo (or stepper) motors, linear servomotors and hydraulics. Rotary motors are the most common choice and could provide large motion angles, but have the disadvantage of linkage backlash in motions with aggressive starts and stops. Also, the model pivot point would not be adjustable purely in software. This favors direct linear actuation. Electric linear motors were selected in favor of hydraulics, on account of the small rig scale and the savings in required support equipment.

2.3. Airfoil model

The airfoil model is 152.4mm chord and nominally 450mmspan, and in cross-section a 0.89mm-thick shell of 316-series stainless steel. It was cut by wire-EDM from five 10cm-thick blocks, with the resulting shell segments welded end-to-end. As installed, there is a 1mm gap between each wingtip and the respective tunnel test section sidewall. A schematic of the airfoil and motion conditions is given in Figure 2.

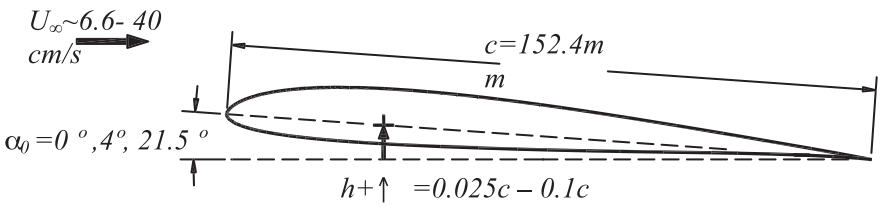

Figure 2. Schematic of SD7003 airfoil, showing range of motion parameters

The rig, tunnel and model are shown in Figure 3. In the photograph, the model is inside the test section, but the glass walls are not visible.

Figure 3. SD7003 airfoil installed in HFWT test section, with plunge rods in position prior to a run (left); Horizontal Free-surface Water Tunnel (middle); and schematic of pitch/plunge rig and airfoil model (right).

2.4. Particle Imaging Velocimetry

Particle image velocimetry data was acquired by triggering off of an external pulse train derived from the position encoders of the motion rig, thus allowing for selection of motion phase at which to acquire data, and for phase averaging. PIV pairs were taken once per period of oscillation, for two sequences of 120 periods each. These were repeated for 4 equally-spaced phases of airfoil motion. For phase-averaging, the first 5 periods were removed from each data set, to exclude startup transients. Vorticity was calculated by explicit differentiation of cubic spline fits to the velocity field (as discussed by Willert and Gharib[20], and implemented by Jeon[21]). The hardware suite included a PCO 4000 11Mpix camera run in single A-D mode and a New Wave Solo-PIV Nd:YAG double-pulsed laser (nominally 125mJ/pulse).

The laser sheet created was approximately 2 mm thick and 45 cm wide at the midpoint of the flow field of interest. Titanium dioxide (TiO_2) was used as the seed material. TiO_2 particles are insoluble in water, have a specific gravity of 4 (water = 1), and a nominal diameter of 2-3 micrometers. Due to the small particle size, the settling velocity of TiO_2 is two orders of magnitude lower than the velocity of the water in the tunnel. For the tunnel velocities and duration of this experiment, the inertial effects of TiO_2 tracer particles were neglected, in accord with the usual practice. TiO_2 particles do have the disadvantage of accreting on the airfoil surface, requiring frequent manual cleaning.

Typical PIV resolution was 110 pixels/cm. For 32x32 pixel windows with 16x16 overlap, this results in 105 vectors per chord. Because of laser reflections from the model surface (painted flat-black) and lack of corrections for PIV windows which at least partially intersect with the model surface or for pixel regions saturated due to laser reflections, data closer than one window length to the airfoil wall – approximately 0.02c – are not reliable and comparisons between CFD and PIV are limited to the region outside the attached boundary layer.

For Re = 40,000, k = 3.93 corresponds to a physical frequency of 2.12 Hz and tunnel flow speed of 26.5 cm/s. For Re = 10,000, both the frequency and flow speed were reduced by a factor of four while the amplitude was held constant . The peak-to-peak plunge amplitude was 15.2 mm (ten percent of the chord) and corresponds to a Strouhal number of 0.12. To minimize the influence of spanwise variations in the flowfield, the PIV light sheet was placed at the 3/4 span location; that is, approximately halfway between the plunge rods and the tunnel wall.

2.4. Accuracy of Model Motion Control

Dynamic following error between commanded and attained position vs. time for the plunge rods is shown for the representative case of sinusoidal pure-plunge with $h = 0.05$, $k = 3.93$. For all pure-plunge cases that follow the motion is a cosine wave, so that velocity is continuous from rest. In the example in Figure 4, the motion is a cosine wave, showing the smoothing transient on startup. One half of a period after startup, dynamic following error is seen to be < 0.5% of the motion amplitude. Error peaks at phase locations of maximal acceleration in the sine wave; the frequency content of the error signal shows a peak at the actuation frequency, followed by harmonics. Two sets of data are given – for the forward plunge rod (green) and the aft (black). The position time histories of the two differ because the mean angle of attack of the model is 4°; with the model mounted upside down (pressure-side of the airfoil towards the test section free-surface), the inclination of the model causes relative elevation of aft plunge rod. It should be noted that the data in Figure 4 are for the motor encoder tape. They do not account for free play (however slight) in the plunge rods or elastic deformation of the model.

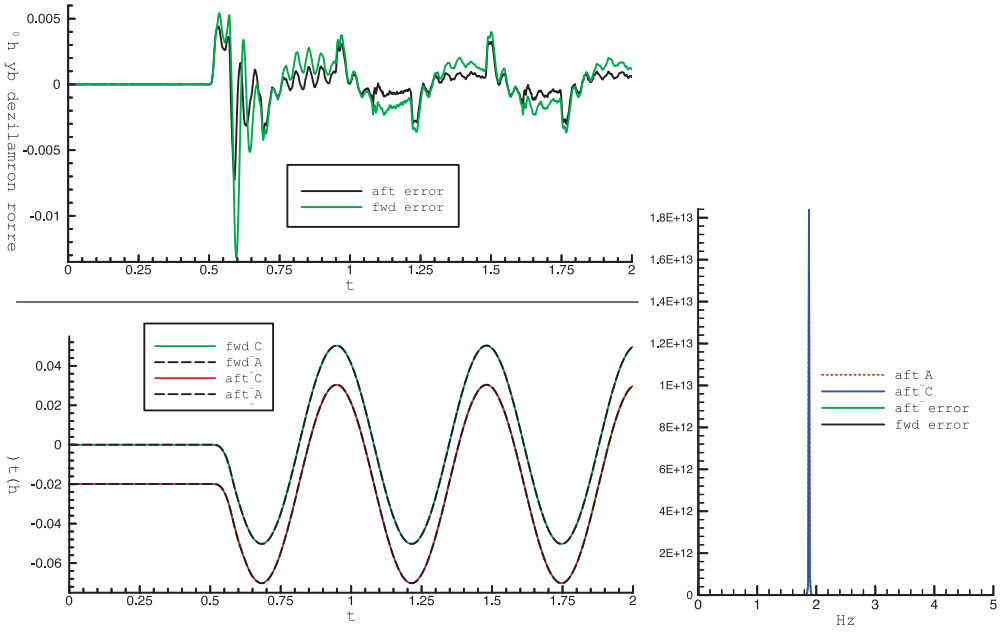

Figure 4. Time-traces of airfoil position and associated errors; difference between commanded and attained position of front and rear plunge rods, normalized by airfoil chord, from motion onset — top left; time traces of plunge rod tip vertical displacement, forward and aft plunge rods, commanded ("C") and attained ("A") — bottom left; and FFT of plunge-rod commanded position, attained position and relative difference (dynamic following error) — bottom right.

3. COMPUTATIONAL METHODS

3.1. The CFL3D code

CFL3D is a thin-layer Navier-Stokes solver developed at NASA Langley Research Center[22]. It is written in the structured framework and is capable of calculating solutions on one-to-one, patched, or overset grids. It also includes convergence acceleration techniques, namely local time step scaling, grid sequencing, and multigrid. It includes built-in routines to accommodate grid motions, including grid deformations. Although several turbulence models are built into the CFL3D code, we use only the Spalart-Allmaras[23] turbulence model. Low-speed preconditioning[24] was not used; instead, computations were run at a higher Mach number of 0.2, and computational frequency was adjusted to match the physical frequency of experiment.

The computational grid, shown in Figure 5, consists of 689 nodes in the i^{th}-direction (around the airfoil surface) and 113 nodes in the k^{th}-direction (normal to the airfoil surface). A denser spacing near the airfoil surface was implemented to more accurately predict boundary layer effects. The outer domains of this grid extend to approximately 20 chords radially away from the airfoil in all directions. Airfoil plunge was handled with the grid motion technique implemented in CFL3D[25], where the entire grid moves.

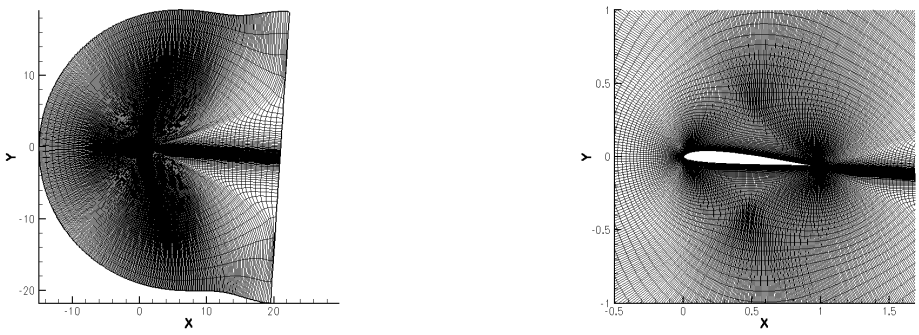

Entire grid Near view of grid

Figure 5. Schematic of grid utilized for CFL3D simulations using moving grid capability.

3.2. The Immersed Boundary Method

The idea of the immersed boundary method is to resolve the flow features around a given geometry embedded in a computational mesh without requiring that the boundary points coincide with mesh nodes. These methods can be useful for complex geometries or moving bodies, avoiding the difficulties of grid adaptation, overset grids, or moving grids. A Cartesian mesh is used, along with the cloud of points defining the airfoil surface. The method implemented here follows that of Mohd-Yusof[26,27], in which the methods developed by Peskin[28] are interpreted as a direct momentum forcing. The effects of the immersed boundary are included by defining band cells surrounding the body, and prescribing conditions at these points, thus mimicking the movement of the surface. The code, developed by Choi et al.[29], solves the incompressible Navier-Stokes equations using the finite volume method. The Spalart-Allmaras turbulence model was also used for the immersed boundary runs.

4. RESULTS

4.1. Frequency and Reynolds number effects

We first consider a qualitative attempt to connect the low-frequency plunge studied by Radespiel et al.[6], with the high-frequency cases considered by Lai and Platzer[7]. Questions include how the near-wake passes from planar, in the quasi-steady case, to nonplanar and reverse-Karman vortex street[7]; what is the role of leading-edge vortex shedding and its coupling into the wake topology; and how the various flow separations depend on Reynolds number.

Figure 6 shows development of the near-wake for k = 0.80 through k = 2.62, for cosine-wave plunge with h = 0.05. Figure 7 extends the reduced-frequency range to k = 3.93. In both figures, snapshots are at the top and bottom of the plunge stroke. Figure 7 includes both the near-wake and the flowfield over the suction side of the airfoil. Figure 6 is at Re = 60,000, and Figure 7 is at 10,000. In all cases the mean angle of attack is $\alpha_0 = 4^o$, and snapshots were taken at least 5 periods after motion onset, to give good confidence that startup transients have relaxed. Substantiation of this assertion is given further below.

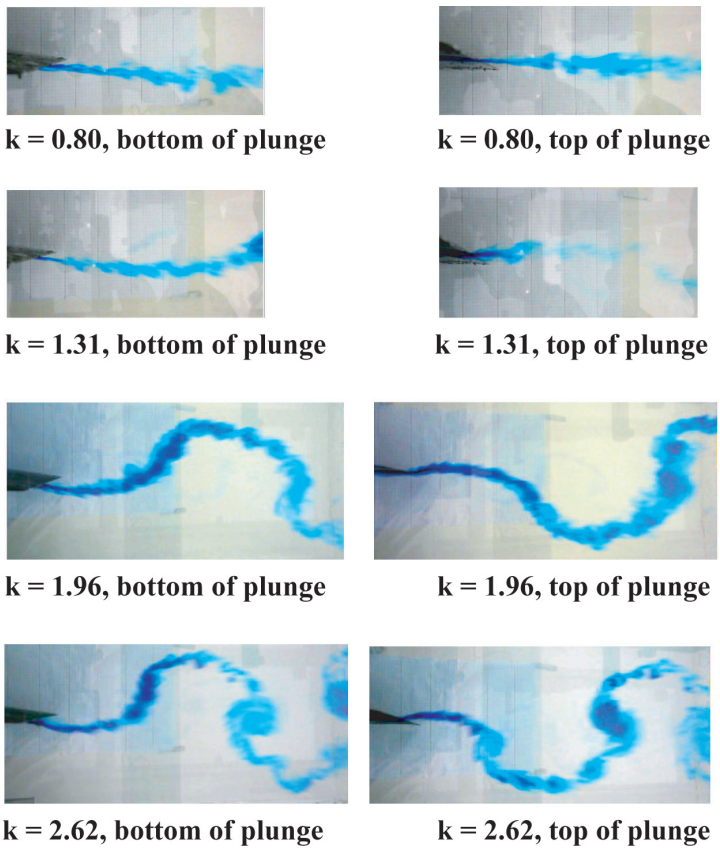

Figure 6. Dye Visualization, Re = 60,000, mean $\alpha = 4°$, h = 0.05: k = 0.080, 1.31, 1.96 and 2.62, at the top (right-hand-side of page, consistent with $\varphi = 0$) and bottom (left-hand-side, consistent with $\varphi = 1/2$).

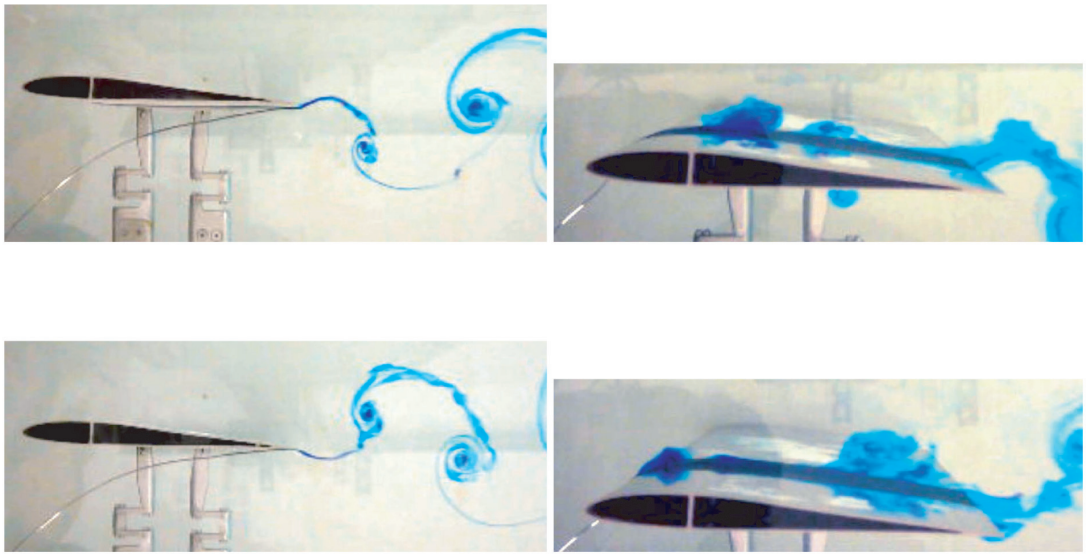

Figure 7. Dye flow visualization for k =3.93, Re = 10,000: near-wake (left) and over the airfoil suction-side (right); top of stroke (upper two images) and bottom of stroke (lower two images).

In Figure 7 the near-wake is rolling up into a reverse-Karman vortex street, much akin to that reported in Refs. 8, 9 and 30, despite the large difference in Reynolds number and airfoil shape, and the nonzero mean angle of attack. Visualization of the flow over the suction-side of the airfoil is by injection just downstream of the leading edge. On the pressure side, visualization of the near-wake is by injection at the trailing edge, also on the pressure side. While for the latter the dye stream is thinner and more coherent, qualitatively the near-wake as resolved by the two injection methods looks similar. We observe, therefore, that the dye injection is not intrusive, despite the obvious presence of the injection probe.

On the suction side of the airfoil, the formation of a small dynamic-stall vortex[31] is discernable, shortly before the bottom of the plunge stroke. This vortex is not shed into the bulk flow, but convects along the airfoil surface essentially at the free-stream velocity. The same vortex from the previous period of oscillation is visible further downstream just ahead of the trailing edge. It does not, however, appear to strongly interact with vorticity shed from the trailing edge, in the form of a merged trailing-edge – leading-edge vortex pair.

Returning to Figure 6, at k = 2.62, the wake is akin to a reverse Karman street, but does not yet evince strong vortex rollup. At k = 1.96 there is still strong wake curvature, but no discernable rollup at all. By k=0.80, the near-wake appears almost planar, although at approximately 10 chord lengths downstream of the trailing edge, a sinusoidal dye streak (not shown) is visible. Interestingly, at low reduced frequency there is no regular Karman vortex street, akin to a bluff body. This is evidently because of the comparatively high Reynolds number (60,000), which is near the on-design condition of this airfoil. In contrast, a NACA 0012 will have clearly discernable Karman-type shedding at conditions where bluff-body-type behavior overwhelms the motion-induced shedding.[32]

It appears, then, to be broadly the case that as reduced frequency increases – while reduced amplitude is held constant – that "Reynolds number effects" become more benign. Indeed, comparing Re = 10,000 – 20,000 – 40,000 – 60,000 for k = 3.93, h = 0.05 at the bottom of the plunge stroke (Figure 8), the near-wake is essentially indistinguishable over this Reynolds number range. Of course, at the higher Re there will be more mass-diffusion, whence the dye streaks will be of lower contrast. There may also be viscous-effects in regions of high shear, such as interior to vortex cores and in the feeding-sheets connecting shed vortices.

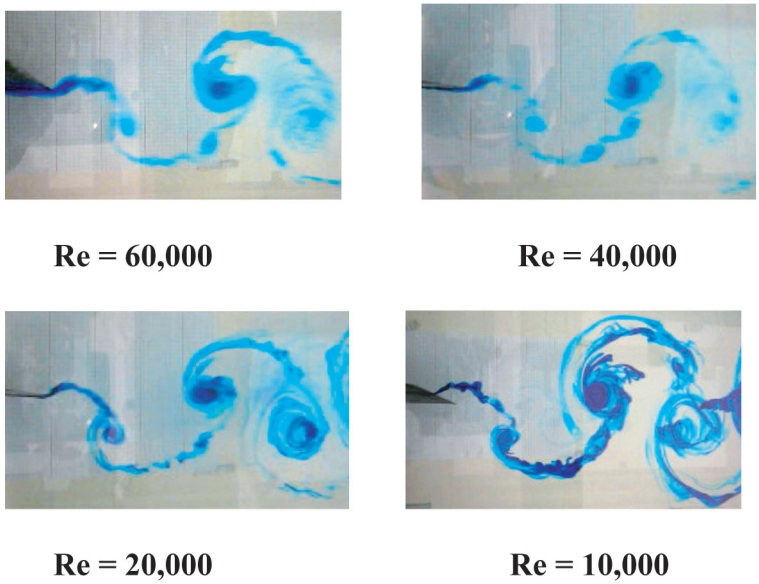

Figure 8. Re = 10,000 to 60,000, mean $\alpha = 4^{\circ}$, h = 0.05: k = 3.93, established flow, top of the plunge stroke $\phi = 0$.

4.2. Plunge at k = 3.93, Re=40,000 and Re = 60,000

We next compare PIV velocity and vorticity results with those of the two computations, for the representative high-frequency case of k = 3.93, h = 0.05. Results are reported for four phases of motion: top of the plunge stroke ($\varphi=0$), halfway on the downstroke ($\varphi=1/4$), bottom of the plunge stroke ($\varphi=1/2$), and halfway on the upstroke ($\varphi=3/4$). At the two halfway phases, the effective angle of attack is just the mean angle of attack – again, $\alpha_T = \alpha_0 = 4^{o}$. At $\alpha=0$, $\alpha_T = \alpha_0 + \text{atan}\,(\dot{h}/U_{\infty}) = 21.5^{o}$, while at $\varphi=1/2$, $\alpha_T = \alpha_0 + \text{atan}\,(\dot{h}/U_{\infty}) = -17.5^{o}$. Static stall for this airfoil, meanwhile, occurs at approximately $\alpha = 11^{o}14$ at Re = 60,000.

Figure 9 compares instantaneous PIV vorticity contour plots with phase-averages, based on 120 image pairs for each, at Re = 40,000. Vorticity was normalized by airfoil chord and freestream velocity, with the near-zero levels blanked off for clarity, and limits set somewhat arbitrarily at ± 36. The region below the pressure-side of the airfoil is also blanked, as it is in the shadow of the PIV light sheet.
While spurious vorticity ("noise") is apparent in the instantaneous images and absent in the phase averages, rendition of concentrated vorticity – over the airfoil suction-side and in the near-wake – is very close between instantaneous and phase-averaged, suggesting strong periodicity. This holds even for the discretization of vorticity concentrations in feeding sheets, especially at $\varphi=1/2$.

Comparison of PIV phase averages and computed results for vorticity (Figure 10) show good agreement in vortex core locations, but both computations evince a dissipation that reduces vorticity peak magnitude in going downstream. Neither CFD method accurately captures the discretization of vorticity in the feeding sheet immediately downstream of the trailing edge. The PIV, on the other hand, does not show as sharp a vorticity concentration for wall-bounded structures near the airfoil suction side.

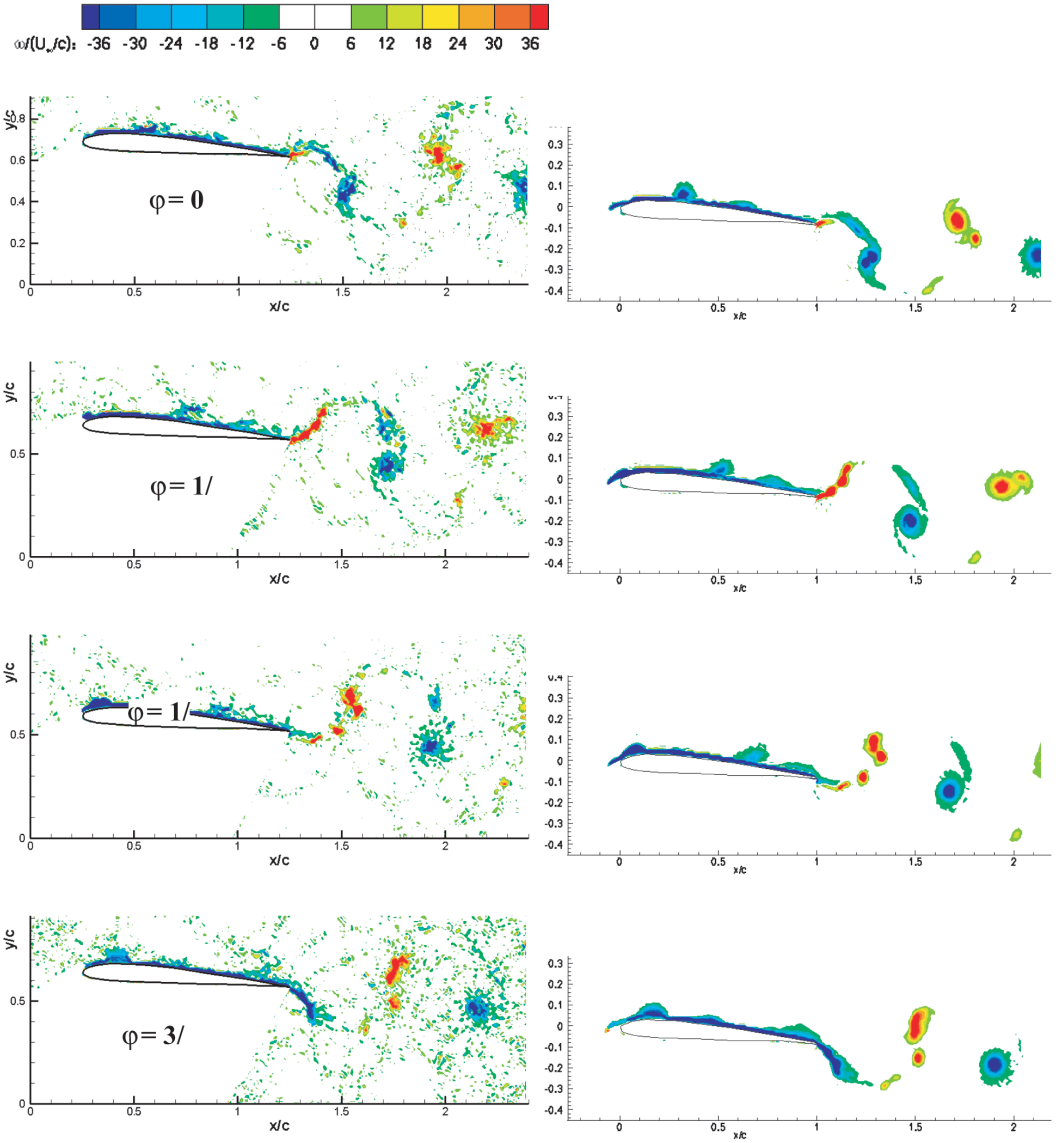

Figure 9. Vorticity contours based on single image pairs for four phases within the cycle. k= 3.93, Re = 40,000.

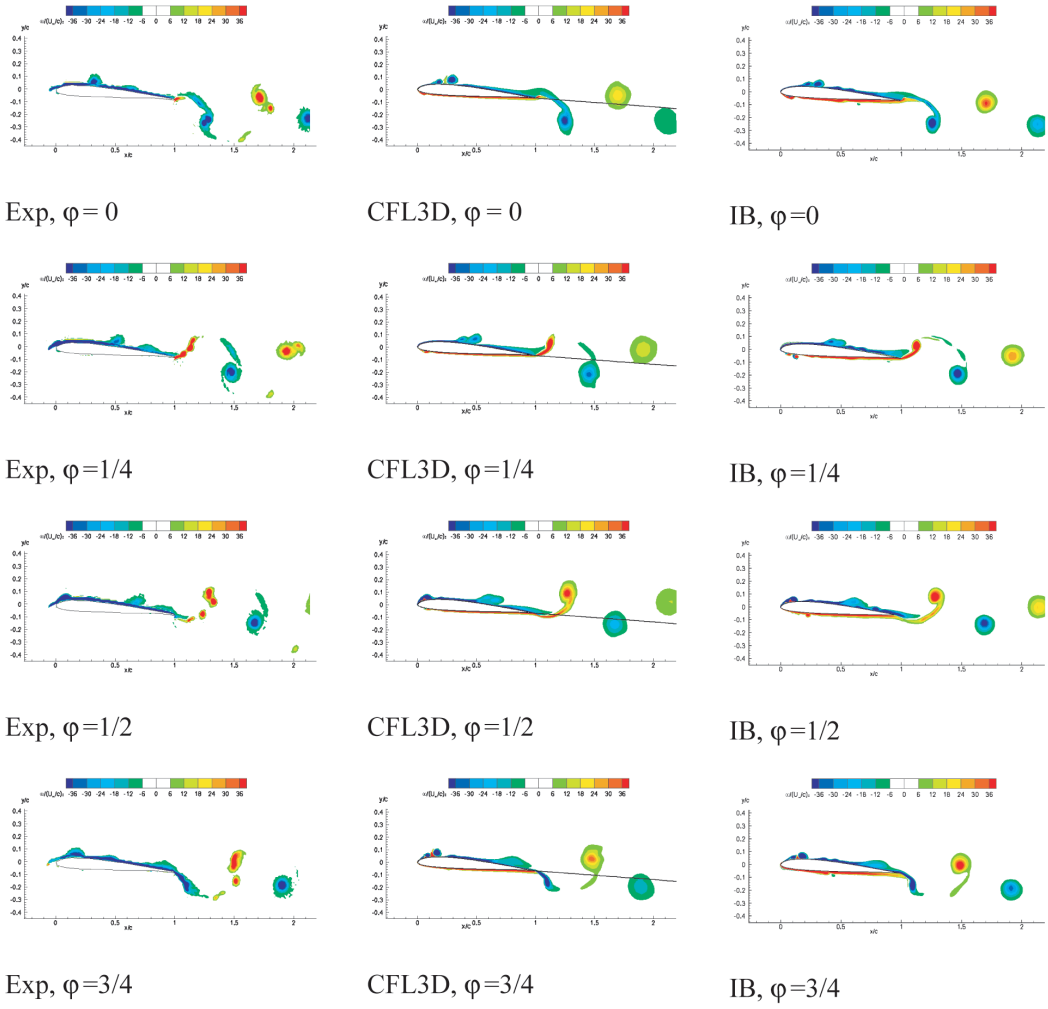

Figure 10. Comparison of vorticity contours from experiment (left column) and two computational approaches [CFL3D (middle column) and immersed boundary method (right column)] at indicated phases of motion; Re=40,000. The color map is the same as that given in Figure 9.

Figure 11 compares the non-dimensional streamwise velocity, u/U_∞ between PIV and CFD. Overall the qualitative agreement amongst all three data sets is excellent. Peak streamwise velocity is on the order of 1.6 u/U_∞ , with a small region of near-zero speed in the feeding sheet from the trailing edge, in the vicinity of where vorticity changes sign.

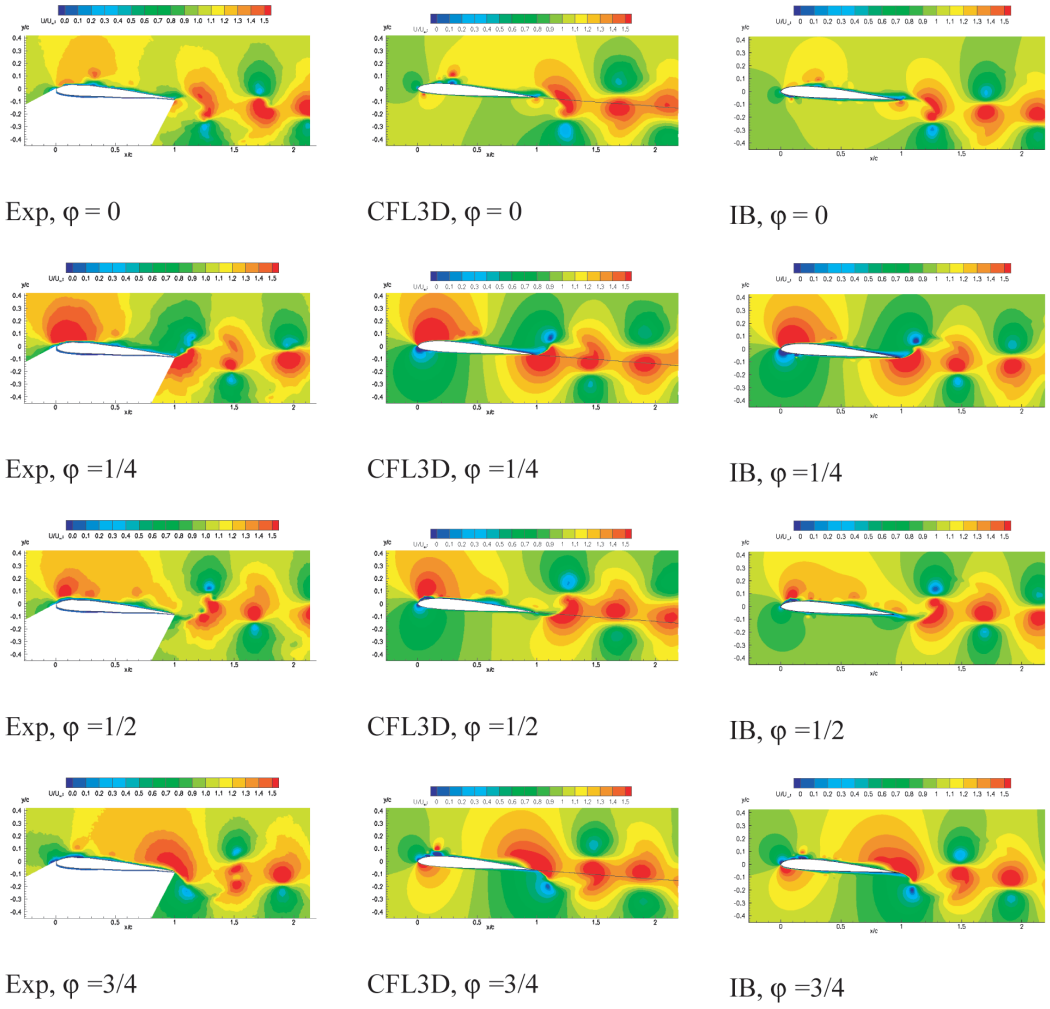

Figure 11. Comparison of streamwise velocity contours from experiment and two computational approaches (CFL3D and immersed boundary method) at various phases of motion; Re=40,000, pure-plunge. The color map extends from $u/U_\infty = 0$ to 1.5.

Figure 12 compares the streamwise velocities in the wake at an x/c location of 2, or one chord length behind the airfoil. There is a good agreement between each of these with the exception of φ=1/2, where there is an extra "peak and valley" in the experimental velocity at y/c=-0.3. The magnitude of the peaks differ significantly at the φ=1/4 location, where evidently dissipation in the computations broadens the y/c-extent of momentum surplus and deficit. The best agreement is when the phase is at F = 3/4, as shown in Fig. 12.

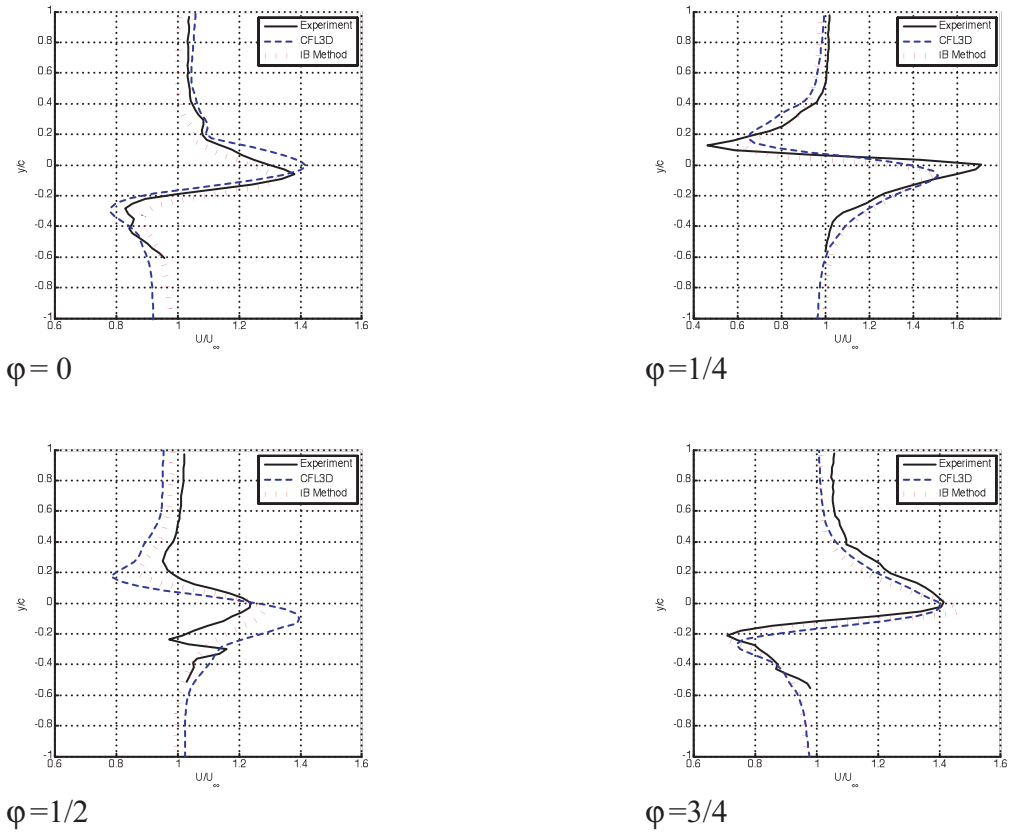

Figure 12. Streamwise-velocity profile in the wake, one chord length behind the trailing edge; Re=40,000.

Phase-averaged PIV vorticity and dye streaklines for Re = 60,000 are compared in Figure 13. For the dye injection, comparison with Figure 7 suggests a Reynolds-number dependency of the size of the "leading edge vortex"; that is, it is smaller for higher Reynolds number. The PIV results shown so far – Re = 40,000 and Re = 60,000 – show little difference, however. We next consider the PIV and computations at Re = 10,000.

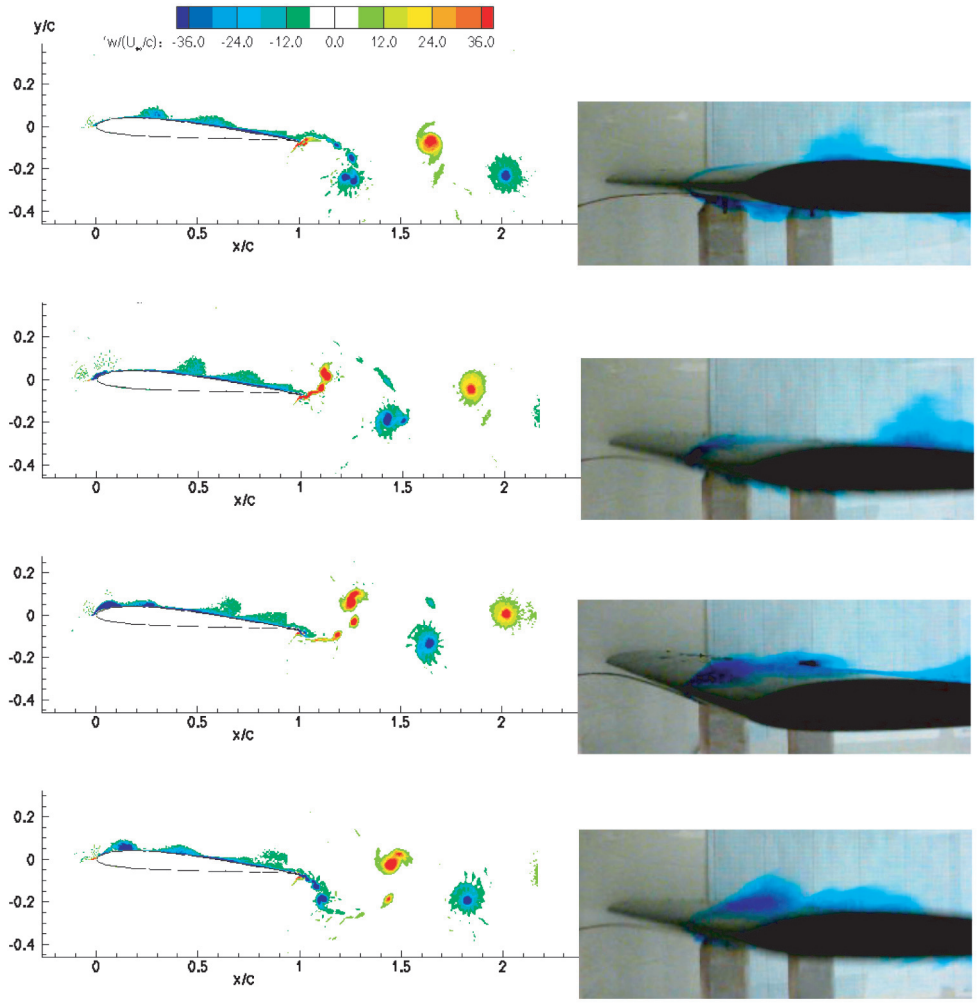

Figure 13. Re = 60,000, k = 3.93, left: phase averaged PIV, right: dye visualization (φ= 0, 1/4, 1/2, 3/4).

4.3. Plunge at k = 3.93, Re=10,000

As with the Re=40,000 cases, the experiment and computation agree well in vorticity contours (Figure 14) and wake-velocity profiles (Figure 15). Consistent with dye injection results in Figure 7 and Figure 13, the leading edge vortex is more pronounced at Re = 10,000, evidently because the suction-side boundary layer is less able to resist the adverse local pressure gradients ultimately responsible for separation. The PIV also confirms the dye injection in the essentially free-stream convection speed of the leading edge vortex in going downstream. This suggests that though the leading edge vortex is nominally wall-bounded, it can be regarded as a discrete vortical structure. The similarities across Re = 10,000 – 40,000 – 60,000 indicate that issues of transition and turbulence in the computation are not of first-order importance in elucidating vorticity in the wake; the computations were all run fully-turbulent. We can not, however, make definitive claim regarding the boundary layer physics vs. Reynolds number, at the presently-available level of resolution. And because the different Re were achieved by proportional increase of tunnel free-stream velocity and the oscillation physical frequency, the evinced Reynolds number insensitivity implies that installation-effects, such as undulations of the free-surface, are not of primary importance either.

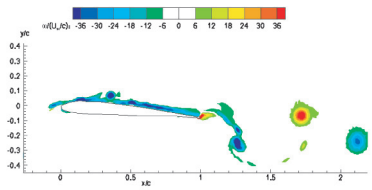

Exp, φ= 0

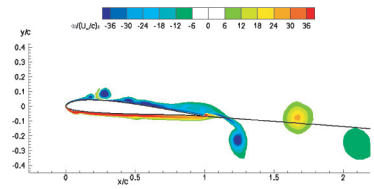

CFL3D, φ= 0

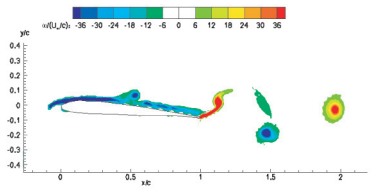

Exp, φ=1/4

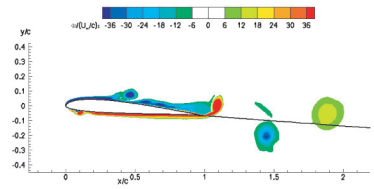

CFL3D, φ=1/4

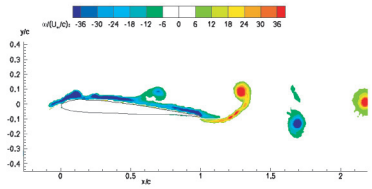

Exp, φ=1/2

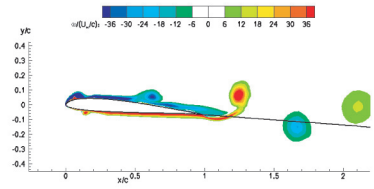

CFL3D, φ=1/2

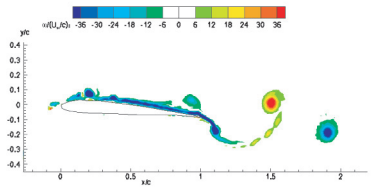

Exp, φ=3/4

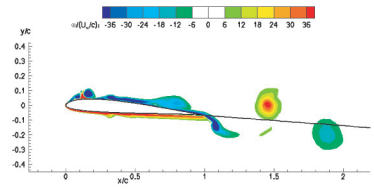

CFL3D, φ=3/4

Figure 14. Comparison of vorticity contours between experiment and computation (CFL3D) for Re=10,000, pure-plunge.

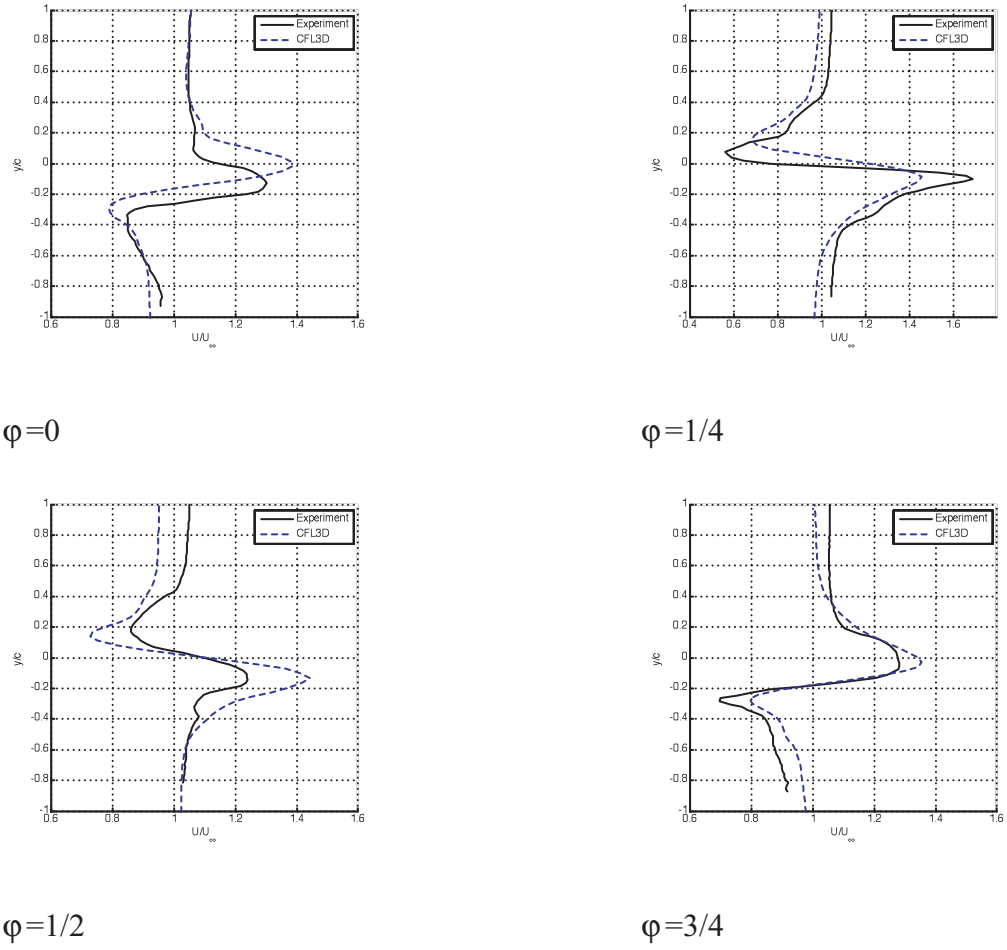

Figure 15. Downstream wake profile comparisons between Experiment and computation (CFL3D); Re=10,000, x/c=2, pure-plunge.

4.4. Strouhal number and reduced amplitude

Lai and Platzer[7] point out for a NACA0012 airfoil in plunge that the production of net wake-like or jet-like momentum aft of the trailing edge varies with the product *kh* (proportional to Strouhal number), and not *k* or *h* individually. However, *h* individually seems to govern the size of shed vortices in the near-wake. The conclusion is broadly the same for the SD7003 with mean $\alpha = 4°$, investigated here. Figure 16 and Figure 17 cover three realizations of (*k*, *h*) each; the former for *kh* = 0.196 (St = 0.125) and the latter for *kh* = 0.591 (St = 0.376). Again, note the mismatch in definition of *k* and St between Refs. [7,8] and the present work. In Figure 16 the starting-flow looks different for the different values of k, while qualitatively the established flow – as instantiated at the top and at the bottom of the plunge stroke – looks broadly invariant; the difference is linear scaling of vortex size, vertical and horizontal separation, which is essentially linear with h. In Figure 17 even the starting-flows for different *k* look qualitatively alike, with the same linear scaling of feature size with respect to *h*. In Figure 17 there is evidence of nonzero mean angle of the wake trajectory, akin to observations made by Jones et al.[8] and Ellenrieder and Pothos[9] for the NACA0012 at zero mean angle of attack. While a cambered airfoil at nonzero angle of attack intuitively suggests a nonzero wake trajectory angle, this happens only for sufficiently high St. Evidently, the wake follows the Strouhal number criteria identified by Jones et al. below a St threshold (~0.3, in the present notation) the wake will be symmetric, and vice versa.[8]

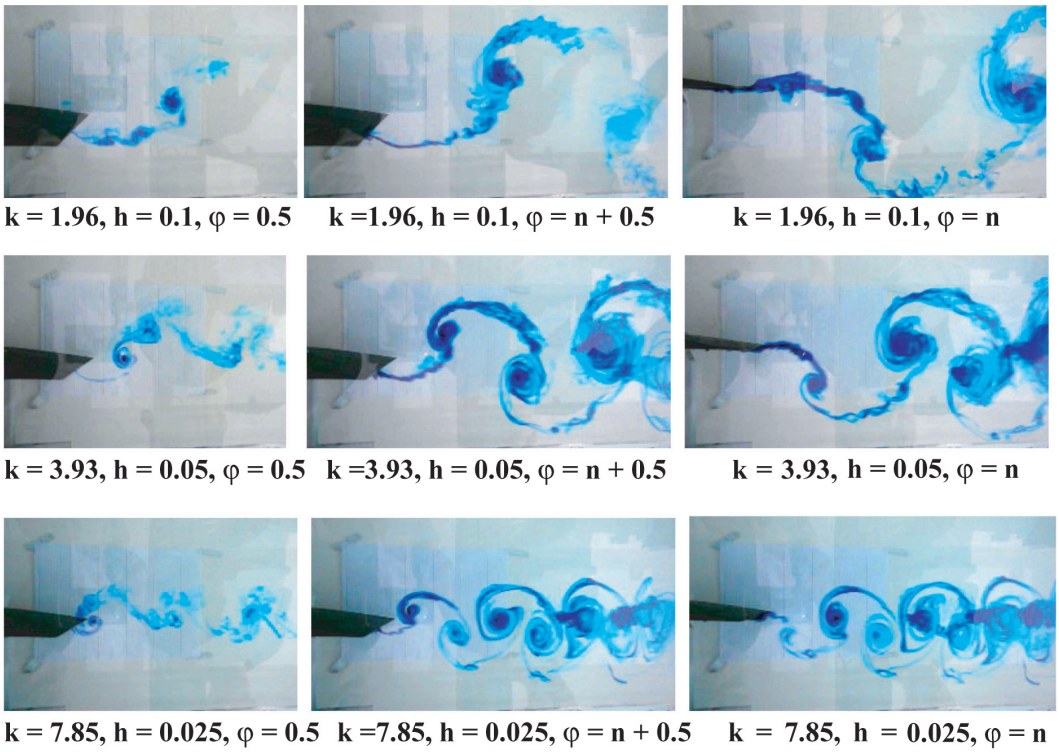

Figure 16. Pure-plunge, Re = 20,000, mean α = 4°; three cases of kh = 0.196, and three motion phases: φ = 0.5 after start-up (bottom of stroke), bottom of stroke in established flow, top of stroke in established flow.

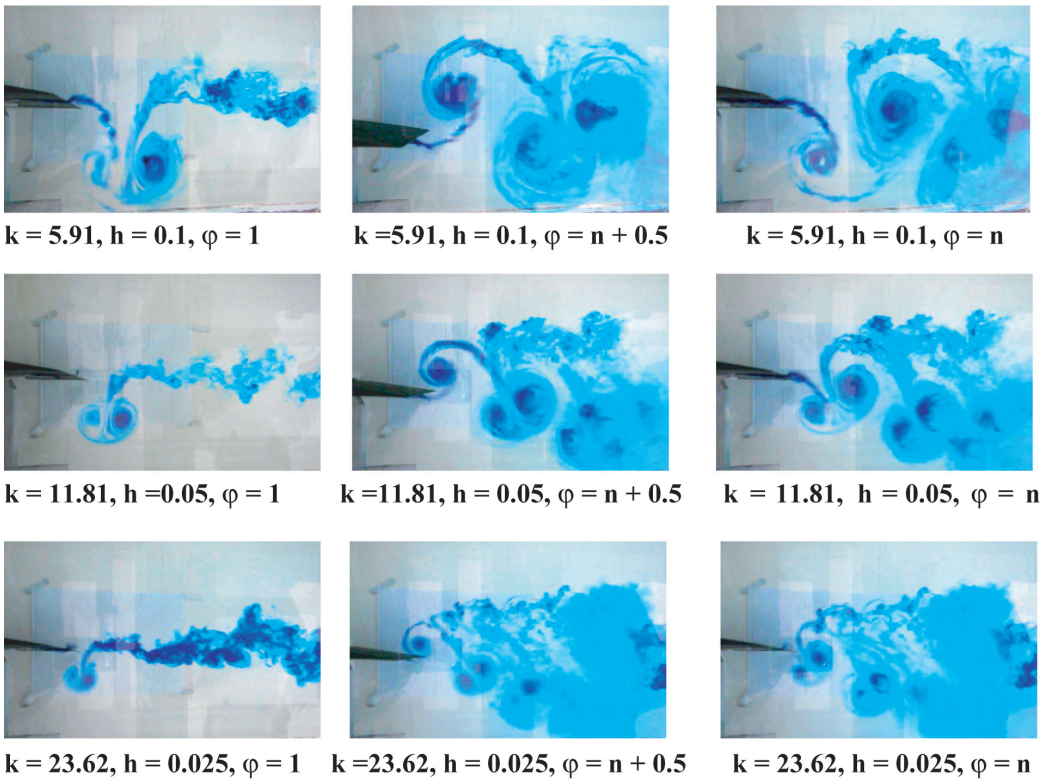

Figure 17. Pure-plunge, Re = 20,000, mean α = 4°; three cases of kh = 0.591, and three motion phases: φ =1 after start-up (top of stroke), bottom of stroke in established flow, top of stroke in established flow.

4.5. Start-up and relaxation to periodicity

While favorable comparison between phase-averages and instantaneous PIV suggests reliable relaxation to periodicity at some time after motion onset, it remains to track how long this relaxation process takes. Figure 18 shows the evolution of the near-wake from motion onset through 10 periods of oscillation, again for k = 3.93, h = 0.05, Re = 60,000. The starting vortex is clearly visible at φ = ½. It convects downstream away from the trailing edge at approximately the free-stream velocity; at φ = 1 after motion onset, its core is ~0.8c downstream of the trailing edge. The starting transient dissipates (the flow relaxes to periodic) by φ ~ 2. This is evidenced by the similarity of the wake at φ = 2 and φ=10. Comparing φ = 3/2 and φ = 3/2, the first vortex pair upstream of the starting vortex – that is, φ= 3/2 – is very similar to its companion pair at φ = 3/2. Evidently, all vortex shedding subsequent to the starting vortex is essentially periodic. This contrasts with the much longer relaxation to periodicity for higher-amplitude motions at the same reduced frequency[4], implying a Strouhal number dependency as well as a reduced-frequency dependency.

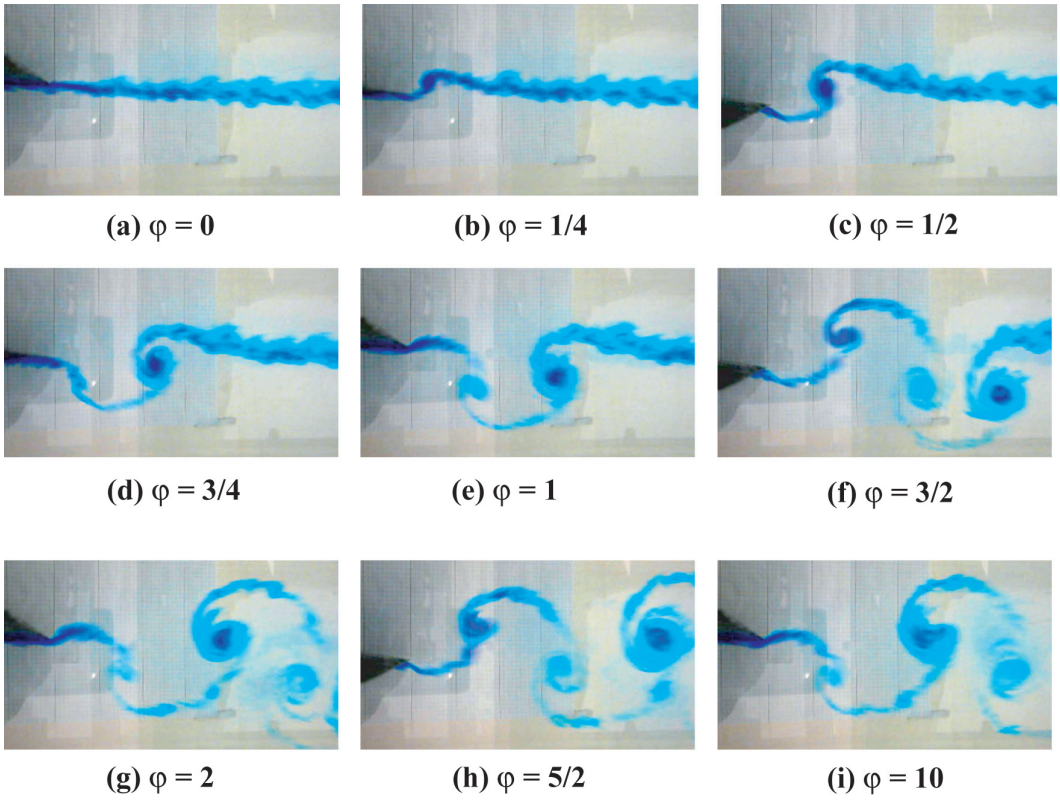

Figure 18. Dye streaklines for near-wake, h = 0.05 k = 3.93 plunge; evolution of starting-flow across 10 periods of motion. Re = 60,000.

4.6. Nonzero mean angle of attack

The present study was in part an outgrowth of work on steady-state airfoil laminar separation bubbles, focusing on a cruise-type angle of attack of α = 4°.[14] Most pitching/plunging studies have been for mean α = 0° and for symmetric airfoils (NACA0012 is justifiably popular). The principal pure-plunge case, k = 3.93 and h = 0.05, is revisited at Re = 20,000 for mean α = 0°, 4° and 21.5° (Figure 19) – the latter being the increment of induced- α from the plunge itself, at the point of maximal vertical velocity. The α = 0° and 4° cases are similar, with the exception that dye streaks are rather finer for α = 0°. The α = 21.5° case shows strong interaction between the vortex shedding and the viscous wake of the airfoil, in the bluff-body sense.

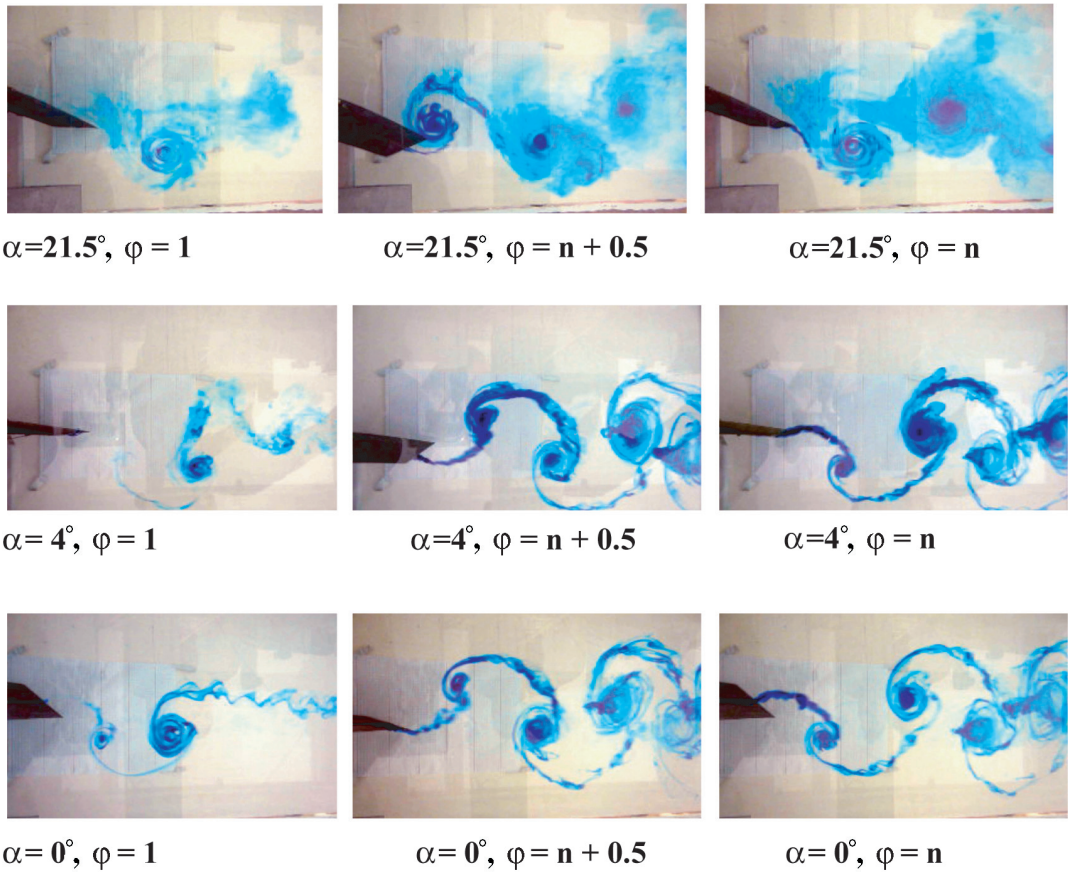

Figure 19. Pure-plunge, Re = 20,000, mean α = 21° (top row), 4° (middle row) and 0° (bottom row); h = 0.05, k = 3.93; left column: φ =1 after start-up (top of stroke); middle column: bottom of stroke in established flow; right column: top of stroke in established flow.

With increasing mean angle of attack, to visualize both the vortex shed from the upstroke and the vortex from the downstroke requires more vigorous injection of dye; otherwise the downstroke-vortex will be preferentially tagged. At α = 4° this effect is moderate (compare the φ =1 α = 4° and α = 0° cases, and the apparent absence of the clockwise vortex following the starting vortex for α = 4°); at α= 21° it is pronounced. Fortunately, the rate of dye flow does not appear to affect the trajectory of the vortex cores, suggesting that mismatch of dye injection speed with free-stream speed does not render the instrument intrusive.

5. CONCLUSIONS

Comparison of water tunnel dye-injection, particle image velocimetry and computations by two different 2D codes (NASA's CFL3D research code and an immersed boundary method) broadly suggests mutual validation between experiment and computation for a high-frequency small-amplitude plunge of the SD7003 cambered airfoil. Relaxation to periodicity for k = 3.93 and h = 0.05, as suggested by good comparison between instantaneous PIV, phase-averaged PIV and dye injection, occurs in about two periods of oscillation after motion onset. A reverse-Karman vortex street indicative of a propulsive wake – in the present case, a weakly-propulsive wake – was observed after relaxation to periodicity. At moderate Strouhal numbers the vortex trajectory follows the nominal free-stream, but at higher St the wake becomes asymmetric, consistent with the results of Lai and Platzer for the NACA 0012. Thus, small nonzero mean angle of attack and airfoil nonzero camber do not cause significant departure from established results for a plunging NACA0012 at high frequency and low amplitude.

Broad accord with results in the literature, such as those of Radespiel et al. and Lai and Platzer, supports the operational validity of 2D, fully turbulent codes in resolving the strength and position of shed vortices in high-frequency but fairly low-amplitude oscillations. This also gives reason to believe that the effects of a relatively intrusive model mounting, where the support rods bisect the pressure-side of the airfoil, do not greatly detract from a flow state commensurate with 2D expectations. However, for the Reynolds numbers studied here, no Karman vortex street was seen at low reduced frequencies, where viscous shedding dominates motion-induced shedding. This suggests that the importance of airfoil shape decreases with increasing reduced frequency.

For flapping-wing MAV design, we can consider the implications of the relative unimportance of airfoil shape, of weakness of Reynolds number effects in the Re = 10,000-60,000 range, of rapid passage to periodicity after motion onset, and of good agreement between fairly traditional 2D CFD methods and PIV. These suggest simplifications in the problems of analyzing wing aerodynamics. However, it should be emphasized that this behavior may be limited to large frequency and small amplitude, and to pure plunge. Larger amplitude motions, motions with more complex kinematics and finite-span effects are just a few of the possible - and highly nontrivial – complications.

The views expressed in this article are those of the authors and do not reflect the official policy or position of the United States Air Force, Department of Defense, or the U.S. Government.

REFERENCES

1 Leishman, J.G. *Principles of Helicopter Aerodynamics*. Cambridge University Press, 2000.

2 von Karman, T., and Sears, W. R., "Airfoil Theory for Nonuniform Motion," *Journal of the Aeronautical Sciences*, Vol. 5, No. 10, 1938, pp. 379–390.

3 McCroskey, W.J., "The Phenomenon of Dynamic Stall," NASA TM 81264, 1981.

4 Ol, M, Dong, H., and Webb, C., "Motion Kinematics vs. Angle of Attack Effects in High-Frequency Airfoil Pitch/Plunge," AIAA-2008-3822

5 Mueller, T.J., "Low Reynolds Number Vehicles," AGARDograph No. 288, 1985.

6 Radespiel, R., Windte, J., and Scholz, U., "Numerical and Experimental Flow Analysis of Moving Airfoils with Laminar Separation Bubbles," AIAA 2006-0501, 2006.

7 Lai, J.C.S., and Platzer, M.F, "Jet Characteristics of a Plunging Airfoil," *AIAA Journal*, Vol. 37, No. 12, pp. 1529-1537, Dec. 1999.

8 Jones, K. D., Dohring, C. M., and Platzer, M. F., "Experimental and Computational Investigation of the Knoller-Betz Effect," *AIAA Journal*, Vol. 36, No. 7., pp. 1240-1246, July 1998.

9 Von Ellenrieder, K.D. and Pothos, S., "PIV measurements of the asymmetric wake of a two dimensional heaving hydrofoil," *Exp. Fluids*, Vol. 44, No. 5, pp. 733-745, 2008.

10 Lian, Y., "Numerical Investigation of Boundary Effects on Flapping Wing Study," AIAA 2009-0539.

11 Kramer, B., "Experimental Evaluation of Superposition Techniques Applied to Dynamic Aerodynamics," AIAA 2002-0700, 2002.

12 Erm, L.P., "Development of a Dynamic Testing System for a Water Tunnel," AIAA 2006-3879, 2006.

13 Kaplan, S., Altman, A., and Ol, M., "Wake Vorticity Measurements for Low Aspect Ratio Wings at Low Reynolds Number," *Journal of Aircraft*, Vol.44, No.1, pp. 241-251, 2007.

14 Ol, M., McAuliffe, B. R., Hanff, E. S., Scholz, U., Kaehler, Ch., "Comparison of Laminar Separation Bubble Measurements on a Low Reynolds Number Airfoil in Three Facilities," AIAA Paper 2005-5149, 2005.

15 Ol, M., "Vortical Structures in High Frequency Pitch and Plunge at Low Reynolds Number," AIAA Paper 2007-4233, 2007.

16 Hanff, E.S. et al., "Final Report: RTO AVT-101 Task Group on Low Reynolds Number Aerodynamics," NATO report, 2007.

17 Parker, K., Soria, J., and von Ellenrieder, K.D., "Characteristics of the Vortex Street behind a Finite Aspect-Ratio Flapping Wing," AIAA 2006-1304, 2006.

18 Anderson, J.M., Streitlien, K., Barrett, D.S., and Triantafyllou, M.S., "Oscillating Foils of High Propulsive Efficiency," *J. Fluid Mech.*, Vol. 360, pp. 41-72, 1998.

19 Kurtulus, D.F., David, L., Farcy, A., and Alemdaroglu, N., "Laser Sheet Visualization for Flapping Motion in Hover," AIAA 2006-0254, 2006.

20 Willert, C.E., and Gharib, M. "Digital Particle Image Velocimetry," *Experiments in Fluids*, Vol. 10, No. 4, January, 1991.

21 Jeon, D. Ph.D. Thesis, Caltech, "On cylinders undergoing one-and two-degree of freedom forced vibrations in a steady flow," 2000.

22 Krist, S. L., Biedron, R. T., and Rumsey, C. L., "CFL3D User's Manual," NASA TM 208444, 1998.

23 Spalart, P. R. and Allmaras, S. R., "A One-Equation Turbulence Model for Aerodynamic Flows," AIAA Paper 92-0439, 1992.

24 Edwards, J. R. and Thomas, J. L., "Development and Investigation of $O(Nm^2)$ Preconditioned Multigrid Solvers for the Euler and Navier-Stokes Equations," AIAA Paper 99-3263, 1999.

25 Bartels, R. E., "Finite Macro-Element Mesh Deformation in a Structured Multi-Block Navier-Stokes Code," NASA TM-2005-213789, July 2005.

26 Mohd-Yusof, J., "Development of Immersed Boundary Methods for Complex Geometries," *Center for Turbulence Research Annual Research Briefs*, 1998, pp. 325-336.

27 Mohd-Yusof, J., "Combined Immersed Boundaries/B-splines Methods for Simulation of Flows in Complex Geometries," *Center for Turbulence Research Annual Research Briefs*, 1997, pp. 317-327.

28 Peskin, C. S., "Flow Patterns Around Heart Valves: A Numerical Method," *Journal of Computational Physics*, Vol. 10, No. 2, October 1972, pp. 220-252.

29 Choi, J.-I., Oberoi, R. C., Edwards, J. R., and Rosati, J. A., "An Immersed Boundary Method for Complex Incompressible Flows," *Journal of Computational Physics*, Vol. 224, No. 2, June 2007, pp. 757-784.

30 Young, J., and Lai, J.C.S., "Oscillation Frequency and Amplitude Effects on the Wake of a Plunging Airfoil," *AIAA Journal*, Vol. 42, No. 10, 2004. pp. 2042-2052

31 McAlister, K.W., and Carr, L.W., "Water Tunnel Visualization of Dynamic Stall," *Journal of Fluids Engineering*, Vol. 101, pp. 376-380, Sept. 1978.

32 Koochesfahani, M.M., "Vortical Patterns in the Wake of an Oscillating Airfoil," AIAA J. Vol. 27, No. 9, pp. 1200-1205, Sept. 1989.